

# Exceptional Tunability over Size and Density of Spontaneously Formed Nanoparticles via Nucleation Dynamics

Jun Kyu Kim,<sup>§</sup> Yong-Ryun Jo,<sup>§</sup> Seunghyun Kim, Bonjae Koo, Jun Hyuk Kim, Bong-Joong Kim,\* and WooChul Jung\*

Cite This: *ACS Appl. Mater. Interfaces* 2020, 12, 24039–24047

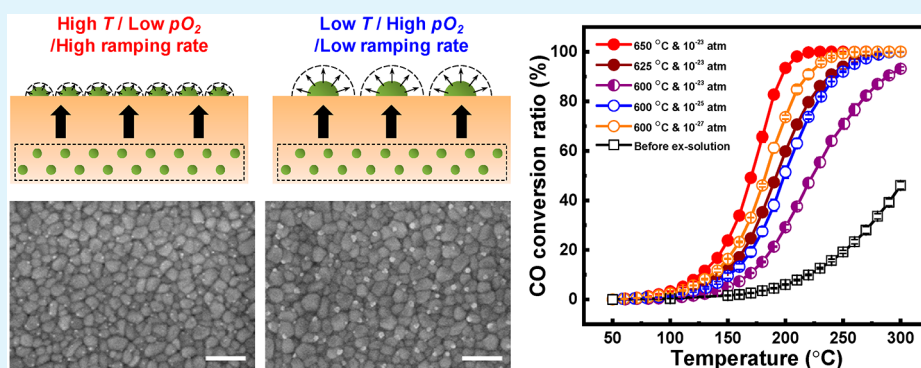
Read Online

ACCESS |

Metrics & More

Article Recommendations

Supporting Information



**ABSTRACT:** The ex-solution process, in which metal nanoparticles are grown on a host oxide, can be used to synthesize nanocatalysts with excellent thermal and chemical durability via spontaneous heterogeneous nucleation. However, this technique lacks a means to control the particle size and density because the amounts of ex-solved metal elements vary with the reduction conditions. Here, we devise a strategy to achieve small particle sizes and high particle densities concurrently by controlling the temperature ( $T$ ), oxygen partial pressure ( $pO_2$ ) and ramping rate of the temperature. Quantitative analyses of Co particles ex-solved on  $Sr_{0.98}Ti_{0.95}Co_{0.05}O_{3-\delta}$  thin films using *ex situ* SEM and *in situ* TEM reveal that the increasing  $T$  and decreasing the  $pO_2$  lead to smaller particle sizes with higher density levels and *vice versa*, contrary to common ex-solution examples. We find that nucleation thermodynamics dictates such counterintuitive behaviors of particle characteristics, which are attributed to our specific ex-solution conditions in which particle interactions are minimized and all the Co atoms are ex-solved under highly reducible conditions. We also demonstrated the feasibility of our strategy via CO oxidation with typical powder-based catalysts, suggesting that this method can be extended to various chemical/electrochemical applications.

**KEYWORDS:** ex-solution, nucleation, particle-size distribution, oxygen partial pressure, CO oxidation

## INTRODUCTION

Heterogeneous catalysts are an essential ingredient for the development of the chemical industry, specifically in the areas of petroleum refining, automobile exhaust treatments, catalytic combustion, and electrochemical devices,<sup>1–8</sup> in which supported catalysts have become part of the mainstream. Supported catalysts can be obtained by dispersing transition metal nanoparticles on supports. In such systems, the metal particles are not consumed during on-stream catalysis and can therefore be recycled. However, the poor thermal resistance of nanoparticles severely limits their longevity as catalysts at elevated temperatures; accordingly, stabilizing the size and distribution of nanoparticles on supports has been considered as the “holy grail” in the field of heterogeneous catalysis.<sup>4,6,9–15</sup>

In this context, the discovery of a metal nanoparticle ex-solution from a parent oxide support suggests a near-ideal solution to heterogeneous catalysis. By employing a complex

metal-oxide support, more reducible metal cations can be selectively extruded onto the oxide scaffolds during partial reduction heat treatments. This process results in unique nanoparticle geometries that are socketed to the host lattice. Due to such a cavity structure, ex-solved metal particles become fastened with strong metal–support-interactions, which results in nanocatalysts with exceptional thermal resistance properties and a good chemical durability.<sup>16–21</sup> Moreover, the technique has an advantage over conventional particle synthesis/dispersion processes, as it can be conven-

Received: March 20, 2020

Accepted: April 28, 2020

Published: April 28, 2020



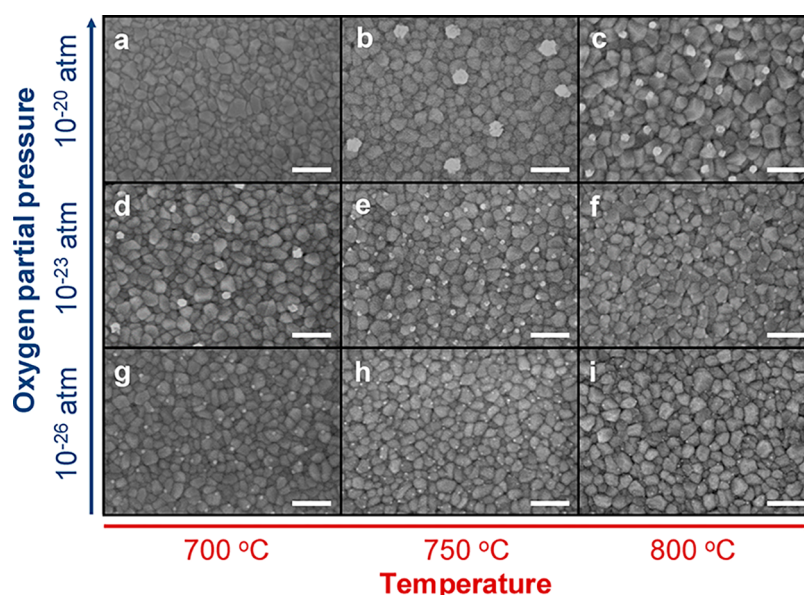


**Figure 1.** Controlled sizes and densities of Co particles ex-solved on  $\text{Sr}_{0.98}\text{Ti}_{0.95}\text{Co}_{0.05}\text{O}_{3-\delta}$  (STC) thin films at various temperatures and oxygen partial pressures. (a–i) Scanning electron microscope (SEM) images of STC thin films in terms of temperatures and oxygen partial pressures. (e.g., (a) shows SEM images of the STC surface after annealing at 700 °C and with the oxygen partial pressure set to  $10^{-20}$  atm for 10 h). The scale bars are 200 nm.

iently achieved in real time with a single heat treatment. Due to the aforementioned merits, the ex-solution method has garnered significant attention from those involved in high-temperature catalysis and renewable energy.<sup>21–41</sup>

Over the past several years, numerous attempts have been made to demonstrate effective catalysis by utilizing the ex-solution phenomenon as a central platform. From these efforts, the viability of this technique is not in doubt, but fundamental information pertaining to the ex-solution process is a pending issue. Indeed, the amount of research on the detailed mechanisms of particle formation and/or the associated growth kinetics is limited. Therefore, little is known about how to control the size and density of the ex-solved particles. Nonetheless, valuable clues regarding the ex-solution process have been found by utilizing well-defined thin-film oxides as model systems. For example, in recent reports,  $\text{La}_{0.2}\text{Sr}_{0.7}\text{Ti}_{0.9}\text{Ni}_{0.1}\text{O}_{3-\delta}$  epitaxial thin films were used to observe the ex-solution behavior of Ni, which sensitively depended on the strain and orientation of the films.<sup>42,43</sup> In more detail, it was suggested that the lattice strain and atomic orientations of the films could significantly alter the nucleation barriers for Ni, determining the nucleus size and the distribution (and thus the density) of the ex-solved particles. In addition, our group recently reported that the grain boundaries and corners of the polycrystalline host oxide films could be favorable heterogeneous nucleation sites and fast cation diffusion pathways for the ex-solution of transition metals,<sup>20,44</sup> thereby offering a means to control the size and density of the produced transition metal particles depending on the grain boundary density. However, manipulating the ex-solved particle size and density via external stimuli such as the temperature and oxygen partial pressure is not straightforward. For instance, most previous studies<sup>16,27,45</sup> have indicated that enhancing the reduction condition (i.e., increasing the temperature and/or hydrogen gas concentration) led to increased particle sizes and decreased particle density levels, and *vice versa*. Thus, such tendencies challenge us to adjust the degree of reduction to

find the ideal condition for maximum catalytic activity (i.e., smaller particle sizes with higher density levels).

Here we report a unique ex-solution regime in which both small particle sizes and high particle density distributions are simultaneously achieved by adjusting the temperature ( $T$ ), oxygen partial pressure ( $p\text{O}_2$ ), and the ramping rate of the temperature. Our observations and analyses show that Co particles ex-solved on  $\text{Sr}_{0.98}\text{Ti}_{0.95}\text{Co}_{0.05}\text{O}_{3-\delta}$  thin films are tightly socketed at the grain boundaries and corners, thereby minimizing the occurrence of coarsening up to 800 °C. The highly reducible structure of thin films containing A-site deficiencies (2 at% Sr), a limited transition-metal dopant concentration (5 at% Co), and high-free-energy sites (i.e., grain boundaries and corners) enabled all Co atoms in the films to be ex-solved within our reducing conditions (i.e., 700–800 °C and  $p\text{O}_2 = 10^{-26}$  to  $10^{-20}$  atm). These ex-solution conditions allow the nucleation properties to determine the particle sizes and densities. Additionally, we find that our approach is applicable to other systems such as powder-based catalysts through CO oxidation.

## RESULTS AND DISCUSSION

**Physical and Chemical Characterizations of  $\text{Sr}_{0.98}\text{Ti}_{0.95}\text{Co}_{0.05}\text{O}_{3-\delta}$  Thin Films.** In this study,  $\text{Sr}_{0.98}\text{Ti}_{0.95}\text{Co}_{0.05}\text{O}_{3-\delta}$  (STC) thin-film samples were prepared by pulsed laser deposition (PLD) on Si substrates. X-ray diffraction (XRD) data show that polycrystalline perovskites films with random orientations were prepared (Figure S1). The use of relatively thick ( $\sim 200$  nm) films grown on largely lattice-mismatched substrates ( $>28\%$ ) eliminates the effects of lattice strain or textural characteristics. Moreover, the results of atomic force microscopy (AFM) analyses shown in Figure S2b and Table S1 confirm that the thin films used here have very dense and flat surfaces (root-mean-square roughness  $<0.6$  nm and surface area ratio (real surface area/projected surface area)  $\sim 1.0008$ ), which are essential for reliable ex-solution analyses. SEM measurements show that the average grain size of the as-

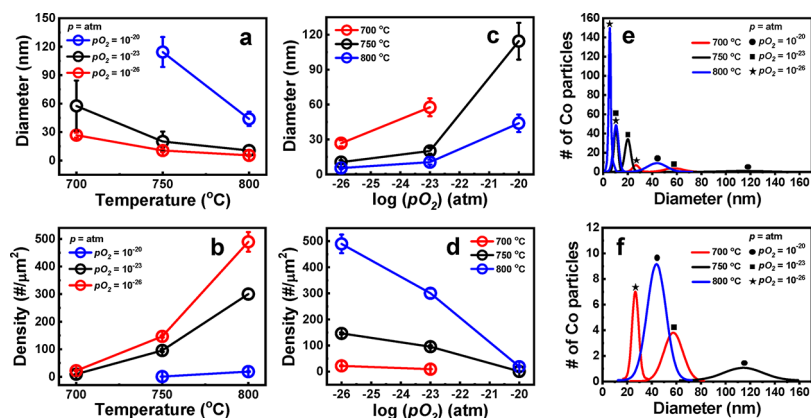


**Figure 2.** Quantitative analyses of ex-solved Co particles in Figure 1: (a–d) Diameter and density of ex-solved Co particles depending on the temperature and oxygen partial pressure ( $pO_2$ ). (e) Size distributions of Co particles on  $Sr_{0.98}Ti_{0.95}Co_{0.05}O_{3-\delta}$  (STC) films. (f) Magnified size distributions of the samples in Figure 2e for peak values smaller than 12. All data were collected from the SEM images in Figure 1. Particles were assumed to be spherical.

deposited STC thin-film samples is  $37.3 \pm 6.7$  nm (Figure S2a), and the sizes remain nearly constant over 800 °C for 10 h ( $39.0 \pm 8.4$  nm), indicating that the grain growth of the host oxide is not significant (Table S1). We also note that 5 at% of Co was doped, and the Sr content in the A site was reduced by 2 at% to promote the Co ex-solution while the crystal structure of the STC remains unchanged under all experimental conditions (see details in Figures S1 and S3). Figure S4 indicates that the chemical compositions of the STC powders and thin films measured by X-ray fluorescence (XRF) and scanning electron microscope-energy-dispersive X-ray spectroscopy (SEM-EDX) have the targeted Co and Ti ratios.

**Dependence of Temperature and  $pO_2$  on the Size and Density of Ex-Solved Co Particles.** To examine the behavior of the Co ex-solution, STC films were annealed at temperatures ranging from 450 °C to 800 °C and at  $pO_2$  levels varying between  $10^{-28}$  and  $10^{-20}$  atm. Figure 1 exhibits a series of SEM images demonstrating how the surface morphology of the STC film changes with the temperature and  $pO_2$  after a 10 h reduction treatment under each condition. In most cases, particles with a wide range of sizes (5–110 nm in diameter) were found on the sample surfaces, induced by the ex-solution process. These particles are primarily located at the grain boundaries or grain corners of the STC films, a typical behavior of heterogeneous nucleation.<sup>20</sup> It is noteworthy that the samples annealed at the lowest temperature (700 °C) and the highest  $pO_2$  level ( $10^{-20}$  atm) show no secondary phases on the surface (Figure 1a) because this condition is not sufficient to reduce Co ions or to nucleate particle on the STC.

We also conducted quantitative analyses of the particles by measuring the particles shown in Figure 1 and other areas (per  $1\,111\,000\text{ nm}^2$ ). Figure 2a–f shows the size, density, and distribution of the Co particles ex-solved on the surface of the STC film (Figure 1a–i) at various temperatures and oxygen partial pressures. As the reduction temperature increases under a constant  $pO_2$  level, the size of the nanoparticles decreases (Figure 2a), while their densities significantly increase (Figure 2b). These trends are in stark contrast to the common behavior of dispersed particles, where at elevated temperatures, particle coarsening becomes significant, and greater amounts of metal elements are ex-solved,<sup>20</sup> causing large particles to appear on the supports.<sup>16,45</sup> Moreover, under a constant temperature, the decrease in the  $pO_2$  value reduces the particle

size (Figure 2c) and increases the particle density (Figure 2d). Additionally, the size distribution was measured; overall, the larger the nanoparticle, the broader the distribution (Figure 2e,f). It should be noted that similar particle size and density trends were also observed with other transition metals (i.e., Ni and Cu) in the films (Figures S5–S7).

**Effects of the Ramping Rate of the Temperature on the Size and Density of Ex-Solved Co Nanoparticles.** We also investigated the growth behavior of ex-solved nanoparticles depending on the heating rate, a process variable that can be readily manipulated during the ex-solution process. Figure 3a–c shows the SEM images of the surfaces of STC films taken after 10 h of annealing under a hydrogen flow when the ramping speeds to 700 °C are set to 1 °C/min, 5 °C/min, and 50 °C/min, respectively. The size and density of the ex-solved Co nanoparticles were measured, as shown in Figure 3d. As the ramping rate increases, the sizes of the particles become smaller, while their density increases (inset of Figure 3d). Moreover, it can be seen that larger particles have wider size distributions. Schematics depicting the particle sizes and densities that are controllable by varying the temperature, oxygen partial pressure, and ramping speed are summarized in Figure 3e, with additional illustrations presented below.

**Real-Time Transmission Electron Microscopy Analyses of Co Ex-Solution Process.** The *ex situ* SEM analyses shown in Figures 1 and 2 are useful when attempting to understand the trends in particle statistics, but these outcomes may not portray quantitative analyses with sufficient accuracy due to the oxidation of particles occurring when the sample exits the annealing chamber. Thus, to prove that the statistics of the ex-solved particles discussed above are unerring, we used *in situ* TEM when temperature (i.e., 450–550 °C) was changed at a given oxygen partial pressure (i.e.,  $pO_2 \sim 10^{-28}$  atm). Figure 4a–c shows representative TEM bright field (BF) images of Co particles ex-solved on the STC films at 450, 500, and 550 °C, respectively after annealing for 30 min under each condition. We find that further annealing does not increase particle sizes, indicating that no additional ex-solution processes or particle coarsening occurs afterward (Figure S8). It is clearly observed that the particles predominantly form at both the grain boundaries and corners. To confirm that the particles are Co crystals, we utilized high resolution TEM (HRTEM) while annealing the sample at 550 °C. An HRTEM

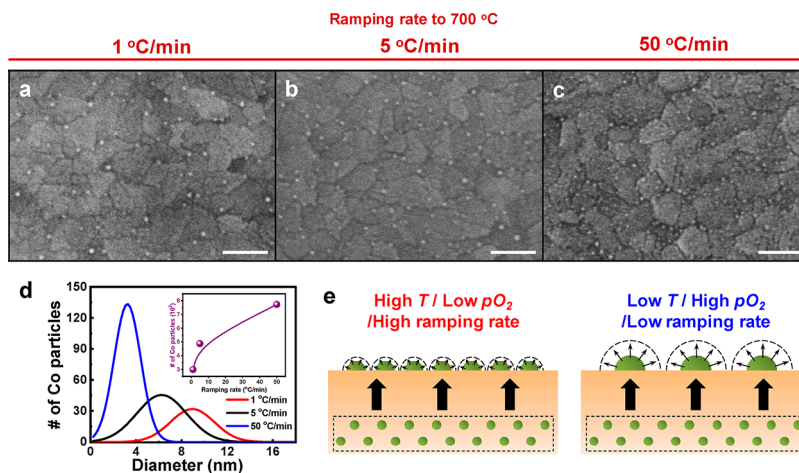


**Figure 3.** Controlled sizes and densities of Co particles ex-solved on  $\text{Sr}_{0.98}\text{Ti}_{0.95}\text{Co}_{0.05}\text{O}_{3-\delta}$  (STC) thin films at various temperature ramping rates: (a–c) Top-view SEM images of STC films after Co ex-solution at various ramping rates of 1, 5, and 50 °C/min to 700 °C under a hydrogen flow, respectively. The scale bars are 100 nm. (d) Size distributions and densities (inset) of Co particles in Figure 3a–c and other areas. (e) Schematics summarizing the effects of the temperature ( $T$ ), oxygen partial pressure ( $p\text{O}_2$ ), and ramping rate on the size and density of ex-solved particles.

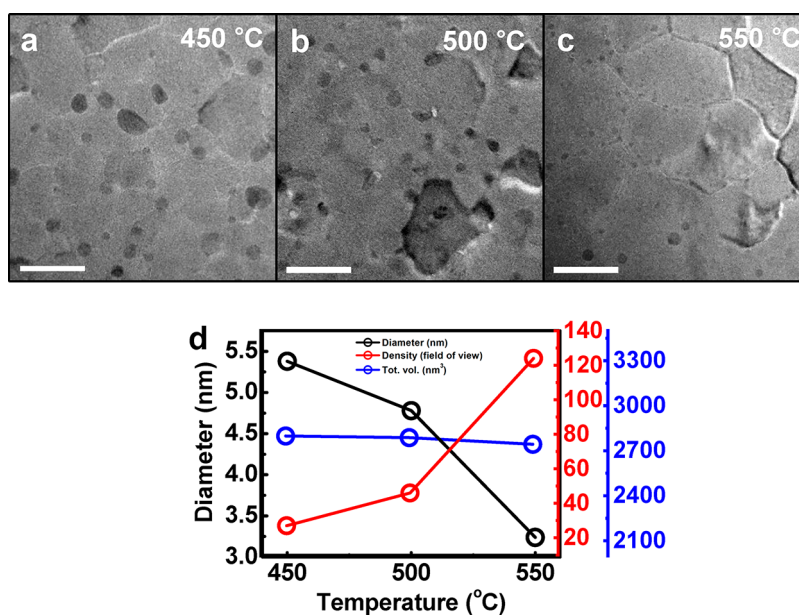


**Figure 4.** *In situ* TEM study of Co ex-solution samples from  $\text{Sr}_{0.98}\text{Ti}_{0.95}\text{Co}_{0.05}\text{O}_{3-\delta}$  (STC) thin films: (a–c) TEM BF images of STC thin films after the complete growth of the Co particles. (d) Diameter (black), density (red), and total volume (blue) of the ex-solved Co particles of the samples in Figure 4a–c, respectively. Scale bars are 30 nm.

image of a single Co particle created at a grain corner is shown in Figure 5a, with fast Fourier transform (FFT) patterns of the boxed regions in Figure 5a exhibited in Figure 5f–i along with the corresponding magnified portions in Figures 5b–e. The FFTs in Figure 5f–h,i were obtained for the three grains and the Co particle, respectively. We find that the crystal structure of the particle (and other particles at other locations) is a face-centered cubic (FCC) type, and the lattice spacings of (111) and (200) are 0.201 and 0.174 nm, respectively, in agreement with those of a pure Co crystal.<sup>49</sup> The FCC structure is thermodynamically preferred above 450 °C.<sup>46,47</sup> It was also found that the surrounding grains have a tetragonal structure and are aligned in different orientations, as indicated by the FFT patterns.

Moreover, quantitative measurements of the particles in Figure 4a–c were carried out, as shown in Figure 4d. From the

plots in Figure 4d, we observe that the particle size/density decreases/increases with an increase in the temperature, precisely coinciding with the *ex situ* results shown above. Additionally, the total volumes of the ex-solved particles on the three samples in Figure 4a–c are nearly identical, and the volumes of Co extruded onto the samples are in good agreement with the doping concentration of Co in each case, indicating that all of the Co atoms in the STC came out of the samples. To check if the Co atoms in the STC films shown in Figures 1 and 2 are exhausted after the reduction process, we carried out energy-dispersive spectroscopy (EDX) measurements of the cross-sectional STC films shown in Figure S9, which are the corresponding weakest and strongest reduction conditions in our experiments, as presented in Figure 1d,i. It is observed that the Co compositions in both samples are nearly zero through the sample thickness, indicating the complete

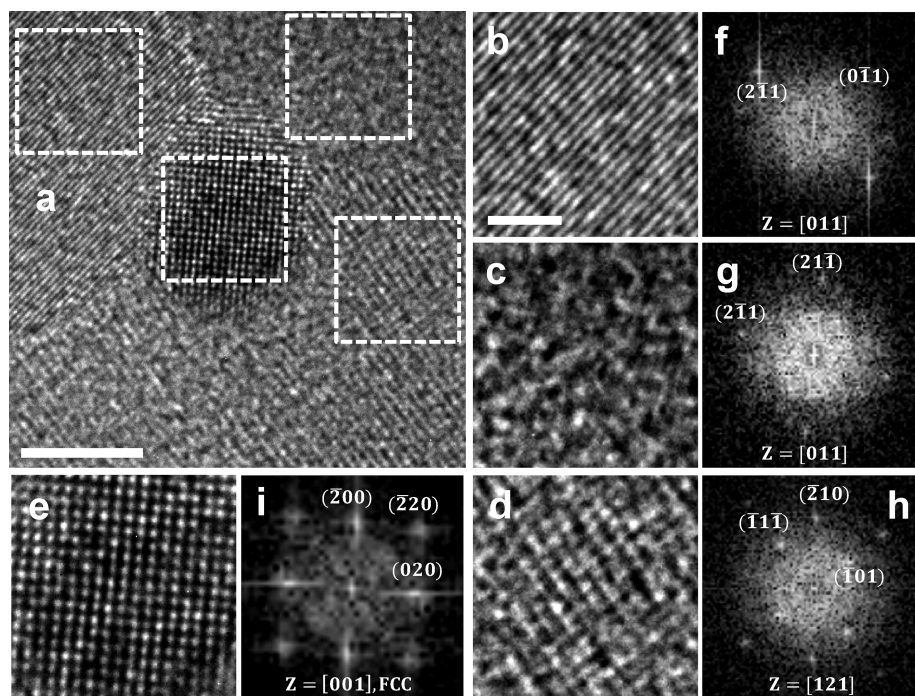


**Figure 5.** Identification of ex-solved Co nanoparticles on  $\text{Sr}_{0.98}\text{Ti}_{0.95}\text{Co}_{0.05}\text{O}_{3-\delta}$  (STC) thin films: (a) High-resolution transmission electron microscope (HRTEM) image of a representative ex-solved Co nanoparticle at a grain corner. Scale bar is 3 nm. (b–e) Magnified images of the boxed regions in Figure 5a: the first three images in Figure 5b–d were taken of the grains at the left, right, and bottom, respectively (clockwise). The last image Figure 5e was taken of the Co particle. (f–i) Corresponding fast Fourier transform (FFT) patterns in Figure 5b–e. Scale bar is 1 nm.

consumption of Co from the STC lattices. This appears to be reasonable because, unlike many previous studies using bulk pellets, our samples were fairly thin (i.e., 200 nm thick). Moreover, the doping concentration of Co was limited only to 5 at%, and the A-site (i.e., Sr) deficiency was also maximized to 2 at%, in which the ex-solution of Co was highly likely.

**Interpretation of the Co Ex-Solution Behavior Using Nucleation Thermodynamics.** The ex-solution phenomenon can be understood as a phase decomposition process at the oxide surface followed by the formation of a second phase via thermal reduction. In fact, a typical second-phase formation process consists of nucleation and growth, and during the growth step, coarsening occurs at elevated temperatures, resulting in the formation of large particles. However, based on the Co ex-solution results shown above, we are in a unique regime in which particle interactions are limited and the total amounts of ex-solved Co atoms are identical regardless of the reduction conditions (i.e., temperature,  $p\text{O}_2$  and ramping speed). Thus, the unusual dependence of the temperature and  $p\text{O}_2$  on the particle size and density discussed above can simply be determined at the initial nucleation stage. According to classical nucleation theory, the nucleation rate of secondary particle formation  $N$  (number of nuclei/ $\text{m}^2 \text{s}$ ) is expressed<sup>50</sup> as follows:

$$N \propto \exp\left(-\frac{\Delta G^*}{kT}\right) \quad (1)$$

Here  $\Delta G^*$  is the critical nucleation energy barrier,  $k$  is the Boltzmann constant, and  $T$  is the temperature. Additionally,  $\Delta G^*$  and the critical nucleus size  $r^*$  can be described<sup>50</sup> as

$$\Delta G^* \propto \frac{1}{(G_i - G_f)^2} = \frac{1}{(\Delta G)^2} \quad (2)$$

$$r^* \propto \frac{1}{G_i - G_f} = \frac{1}{\Delta G} \quad (3)$$

where  $G_i$  and  $G_f$  are the Gibbs free energies of our system before and after Co particle formation, respectively, and  $\Delta G = G_i - G_f$  is the driving force for particle formation and is indicative of the supersaturation of Co atoms on the STC surface. Thus, as our system is exposed to stronger reducing conditions (i.e., increasing temperatures and decreasing  $p\text{O}_2$  levels),  $\Delta G^*$  decreases, thereby increasing the particle density and decreasing the critical nucleus size, consistent with the behavior of the Co ex-solution discussed above. Again, due to the specific conditions of our system, the particles do not continuously grow. Instead, their sizes remain small compared to those under weaker reducing conditions. An identical trend is also observed when the heating rate is altered, as shown in Figure 3. For example, if the heating rate is slow, nucleation may occur while the temperature is rising, in which a smaller  $\Delta G$  is imposed on the system. Thus, the particle size/density increases/decreases.

**Applying the Proposed Strategy to CO Oxidation Catalysis.** The observations thus far demonstrate clearly that the particle size and density in the ex-solution process can easily be controlled by appropriate material selection and reductive heat treatments. As a next step to determine if this method is applicable to the development of realistic high-performance catalysts, we synthesized STC powder samples and monitored the dependence of temperature and gas atmospheres on their surface morphologies and catalytic reactivity levels during reductive heat treatments. Here we chose CO oxidation, which is the basic unit of various industrial chemical reactions, and changed both the temper-

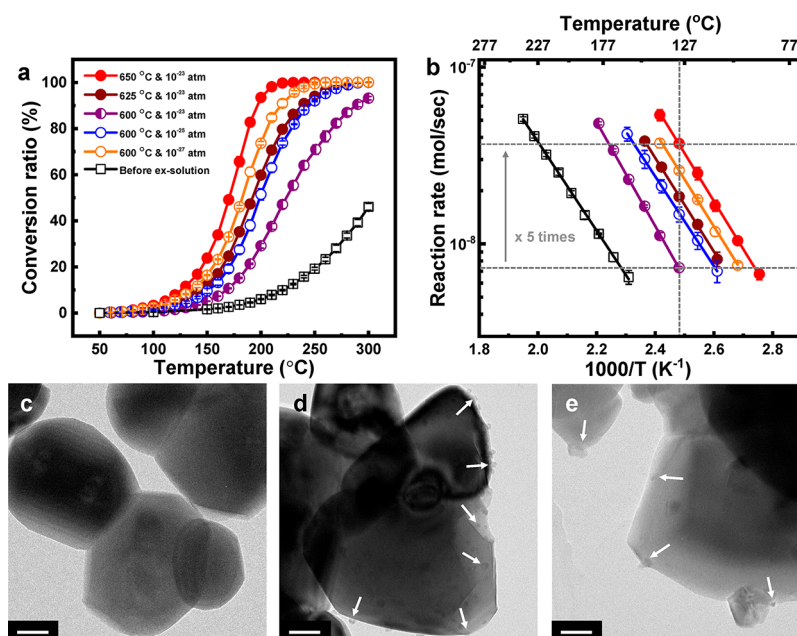


**Figure 6.** Catalytic reactivity of powder-based  $\text{Sr}_{0.98}\text{Ti}_{0.95}\text{Co}_{0.05}\text{O}_{3-\delta}$  (STC) catalysts: (a) Light-off curves pertaining to the CO conversion (CO oxidation) to  $\text{CO}_2$  outcomes with different ex-solution temperatures and oxygen partial pressures ( $p\text{O}_2$ ). (b) Kinetic data for CO oxidation. (c–e) TEM BF images of representative catalyst particles, prior to the ex-solution process, after the ex-solution process at  $600\text{ }^\circ\text{C}$  and  $10^{-27}$  atm  $p\text{O}_2$ , and at  $600\text{ }^\circ\text{C}$  and  $10^{-23}$  atm  $p\text{O}_2$ , respectively. Representative ex-solved Co nanoparticles are indicated with arrows. Scale bars are 50 nm.

ature and  $p\text{O}_2$  from  $600\text{ }^\circ\text{C}$  to  $650\text{ }^\circ\text{C}$  and from  $10^{-27}$  to  $10^{-23}$  atm, respectively.

Light-off curves of CO to  $\text{CO}_2$  conversion for each heat-treatment condition are shown in Figure 6a. For clarity, the sample annealed at  $600\text{ }^\circ\text{C}$ ,  $p\text{O}_2 = 10^{-23}$  atm (purple half-filled circle), is used as a reference, the dependence of the temperature under a constant  $p\text{O}_2$  is presented by filled circles, and the dependence of  $p\text{O}_2$  at the same temperature is represented by empty circles. As shown in Figure 6a, the CO conversion rates of the samples after the ex-solution process under all conditions are remarkably accelerated compared to those prior to the reduction step, proving that Co particles act as CO oxidation catalysts, as expected.<sup>20</sup> Significantly, when the temperature increases at the same  $p\text{O}_2$  or the  $p\text{O}_2$  level decreases at the same temperature, CO oxidation is more strongly activated. In addition, as indicated in the Arrhenius plot in Figure 6b, all samples show similar activation energy ( $E_a$ ) values (42.6–49.4 kJ/mol) regardless of the reducing condition used, whereas the  $\text{CO}_2$  production rate increases dramatically as the temperature increases and the  $p\text{O}_2$  level decreases, as observed by the increase in the prefactors of the plots, which is proportional to the number of active sites.<sup>20</sup> For example, at  $130\text{ }^\circ\text{C}$ , the rate is improved by five times by controlling the reducing conditions (from the purple half-filled circle to the red-filled circle). These results illustrate that the Co particles ex-solved under various reducing conditions are operative under the same mechanism of CO oxidation, whereas the density of the active sites is effectively controlled by changing the temperature and  $p\text{O}_2$ , as explained above. Representative TEM images of STC powders treated under different reducing conditions are shown in Figure 6d,e. It was observed that lowering the  $p\text{O}_2$  ( $10^{-27}$  atm) level at a constant temperature ( $600\text{ }^\circ\text{C}$ ) generates a greater density of ex-solved Co particles on the surface of the powder, in agreement with the aforementioned results.

## CONCLUSION

In summary, the size distribution of ex-solved Co particles according to systematically controlled reducing heat treatments was investigated with a high reliability and reproducibility through flat and dense polycrystalline STC thin films. Notably, we independently manipulated the three key variables, the temperature,  $p\text{O}_2$  level, and ramping rate of the temperature, which led us to find a unique thermodynamic regime in which particle formation can be directly linked to the initial nucleation step. In other words, the overall size and density of ex-solved Co nanoparticles, and therefore the CO oxidation performance can be exceptionally tuned according to the dynamics of the nucleation thermodynamics, even in identical parent solid solutions. Thus, we believe that the strategy presented in this work will facilitate the achievement of an ideal catalytic bed (i.e., maximize the utilization of catalysts with a high mass activity) using the ex-solution process. The importance of nuclei formation, which is the first step in the formation of a new thermodynamic phase, particularly regulated by the oxygen chemical potential and thermal energy, challenges the current paradigm of ex-solved catalyst design, which has been overwhelmingly focused on performance demonstrations.

## METHODS

**Thin-Film Sample Preparation.**  $\text{Sr}_{0.98}\text{Ti}_{0.95}\text{Co}_{0.05}\text{O}_{3-\delta}$  (STC) powders were synthesized by the traditional solid-state reaction method. Conventional powders of  $\text{SrCO}_3$  (Sigma-Aldrich, 99.9%) and  $\text{TiO}_2$  (Sigma-Aldrich, 99.8%) were used as the host  $\text{SrTiO}_3$  oxide precursors, and the conventional powder of  $\text{Co}_3\text{O}_4$  (Alfa Aesar, 99.7%) was used as a metal dopant precursor. Appropriate ratios of precursors were mixed in high-purity ethanol with zirconia balls for 10 h. After mixing, the ethanol was dried on a hot plate and in an oven for 24 h. The completely dried powders were calcined at  $1200\text{ }^\circ\text{C}$  with a ramping rate of  $4\text{ }^\circ\text{C}/\text{min}$  in an ambient air condition for 8 h. The synthesized powders were formed into a green body with a diameter of 1 in. by uniaxial compression at  $\sim 40$  MPa after uniform

grinding. Subsequently, this green body was cold-isotropically pressed at 290 MPa for 15 min and then sintered at 1400 °C for 8 h at a ramping rate of 4 °C/min in ambient air to become the dense target used in the deposition step.

Thin films of STC were deposited on  $1 \times 1 \text{ cm}^2$  Si substrates by pulsed laser deposition (PLD<sup>48</sup>) for an *ex situ* SEM analysis. Additional STC films were also deposited on  $\text{SiN}_x$  membrane TEM grids for *in situ* TEM analysis. A KrF excimer laser (Coherent COMPex Pro 205) was used with a wavelength of 248 nm, an average energy of 210 mJ/pulse, and laser repetition rates of 10 Hz (*ex situ* SEM samples) and 2 Hz (*in situ* TEM samples). During the deposition step, the PLD chamber was maintained at 700 °C (heater temperature) with a 10 mTorr working pressure by pure oxygen gas. Thickness of the thin films was approximately 200 and 25 nm, respectively, for the SEM and TEM analyses. After thin-film deposition, the samples were annealed in the chamber at 700 °C with 1 Torr pure oxygen for 20 min for crystallization of the oxide thin films. As-deposited thin-film samples were annealed in the temperature range of 650–800 °C under buffer gas mixtures with an appropriate ratio of  $\text{H}_2$ ,  $\text{H}_2\text{O}$ , and Ar for 10 h. To control the  $p\text{O}_2$  precisely in real time during the annealing step, the  $p\text{O}_2$  value was measured by a zirconia-based custom-made oxygen sensor. The sensor was connected to the outlet of the reactor and was operated at 800 °C. In addition, an infrared gold image furnace (RHL-E44VHT) was used to anneal the STC films with a wide range of ramping rates.

**Physical Characterization.** The crystal structures of the as-deposited thin-film samples were analyzed using a thin-film X-ray diffractometer (XRD, Ultima IV, Rigaku). XRD was performed in two-theta-scan mode using a  $\text{Cu K}\alpha$  radiation beam source ( $\lambda = 1.54056 \text{ \AA}$ ). The measurement was conducted in the range from 20° to 60° at every 0.01° step with a 4°/min scan speed. JADE 6.0 software was used for processing and identification of the XRD data.

Atomic force microscopy (AFM, XE-100) images of the as-deposited thin-film samples were obtained at a scan rate of 0.98 Hz, and the root-mean-square (RMS) roughness and specific surface area were determined from the AFM images using the Park Systems XEI software. Additionally, the surface morphologies of the as-deposited and annealed thin-film samples were observed using a scanning electron microscope (SEM, Hitachi, S4800). When observing the nanoscaled species, the samples were not coated with osmium or carbon. Additionally, the SEM device was operated at a 3 kV voltage and 7  $\mu\text{A}$  with working distances ranging from 2.0 to 4.0 mm.

The chemical composition of the synthesized powder was characterized by X-ray fluorescence spectrometry (XRF, ZSX Primus II), and that of the thin-film samples was characterized by SEM energy-dispersive X-ray spectroscopy (SEM-EDX, SU8230)

**In Situ Transmission Electron Microscopy Analysis.** The crystal structures of STC thin films and ex-solved Co particles were examined via high-resolution transmission electron microscopy (HRTEM) and fast Fourier transformation (FFT) using a high-resolution transmission electron microscope (TEM, Tecnai G2, F30 S-Twin, operating at 80–300 keV, FEI). The investigation of the evolution and growth of the Co particle ex-solved on the STC films was conducted using an *in situ* gas flow holder (Hummingbird Scientific) within the TEM analytic chamber ( $1 \times 10^{-7}$  Torr). Each targeted temperature was reached in  $10^{-30}$  seconds using an autocontrol mode depending on the targeted temperatures. The  $p\text{O}_2$  level was controlled identically to the *ex situ* works described above.

**How To Determine the Ex-Solved Particle Properties.** We approximated the particle image by an ellipse, and the diameter  $d$  is calculated as the geometric mean of the semimajor and semiminor axes, that is, the diameter of a circle with an equivalent area. To calculate the total volume, we assumed that particles are spherical with the diameter  $d$ . Then we summed the volumes of the particles placed on the specific areas (per  $1111000 \text{ nm}^2$ ) of the STC film. Within the specified areas, we determined the size distributions and the total number of the particles, thus density.

**CO Oxidation Sample Preparation and Measurement.** STC powder-based catalysts for evaluating the reactivity of CO oxidation

were synthesized by the sol–gel method. Appropriate ratios of  $\text{Sr}(\text{NO}_3)_2$  (Sigma-Aldrich,  $\geq 98\%$ ), titanium isopropoxide (Sigma-Aldrich,  $\geq 97\%$ ), and  $\text{Co}(\text{NO}_3)_2 \cdot 6\text{H}_2\text{O}$  (Sigma-Aldrich,  $\geq 98\%$ ) precursors were mixed into DI water with ethylenediaminetetraacetic acid (EDTA, Junsei) and citric acid (Junsei). The metal cations:EDTA: citric acid ratio was set to 1:1:2.5. The solution was homogeneously mixed by stirring it at 170 °C and at pH = 8 until complete gelation. After gelation, it was fired at 450 °C for 3 h and subsequently calcined at 1100 °C for 5 h. The as-prepared powder samples were annealed in the temperature range of 600–650 °C under buffer gas mixtures with an appropriate ratio of  $\text{H}_2$ ,  $\text{H}_2\text{O}$ , and Ar for 1 h. The  $p\text{O}_2$  level was controlled identically to thin-film works described above.

CO oxidation was tested *in situ* with a quadrupole mass spectrometer (Pfeiffer Vacuum GSD320) in a fixed-bed quartz flow microreactor. In the catalytic bed, quartz wool was placed on the bottom layer to prevent the displacement of the catalyst, and 50 mg of catalyst mixed with 100 mg of catalytically inert quartz sand was packed between an additional quartz sand layer. Prior to the measurements, samples were pretreated in 4%  $\text{O}_2$  at 300 °C for 15 min to remove any surface adsorbates. For CO oxidation, 50 sccm in total of the reactant gas was injected into the reactor in a composition of 1% CO, 4%  $\text{O}_2$ , and Ar as a balance gas corresponding to gas hourly space velocity (GHSV) of  $60000 \text{ mL g}^{-1} \text{ h}^{-1}$ . The catalytic activity was measured over the temperature range of 50 °C to 300 °C, and the cycle was repeated three times.

## ■ ASSOCIATED CONTENT

### Supporting Information

The Supporting Information is available free of charge at <https://pubs.acs.org/doi/10.1021/acsami.0c05215>.

Physical and chemical characterizations on  $\text{Sr}_{0.98}\text{Ti}_{0.95}\text{Co}_{0.05}\text{O}_{3-\delta}$  thin films (Figures S1–S4 and Table S1), additional SEM and quantitative results of various metal (Figures S5–S7), *in situ* TEM results (Figure S8), and EDX analyses of  $\text{Sr}_{0.98}\text{Ti}_{0.95}\text{Co}_{0.05}\text{O}_{3-\delta}$  thin films (Figure S9) (PDF)

## ■ AUTHOR INFORMATION

### Corresponding Authors

**Bong-Joong Kim** – School of Materials Science and Engineering, Gwangju Institute of Science and Technology (GIST), Gwangju 61005, Republic of Korea; [orcid.org/0000-0002-5335-4342](https://orcid.org/0000-0002-5335-4342); Email: [kimbj@gist.ac.kr](mailto:kimbj@gist.ac.kr)

**WooChul Jung** – Department of Materials Science and Engineering, Korea Advanced Institute of Science and Technology (KAIST), Daejeon 34141, Republic of Korea; [orcid.org/0000-0001-5266-3795](https://orcid.org/0000-0001-5266-3795); Email: [wjung@kaist.ac.kr](mailto:wjung@kaist.ac.kr)

### Authors

**Jun Kyu Kim** – Department of Materials Science and Engineering, Korea Advanced Institute of Science and Technology (KAIST), Daejeon 34141, Republic of Korea

**Yong-Ryun Jo** – School of Materials Science and Engineering, Gwangju Institute of Science and Technology (GIST), Gwangju 61005, Republic of Korea

**Seunghyun Kim** – Department of Materials Science and Engineering, Korea Advanced Institute of Science and Technology (KAIST), Daejeon 34141, Republic of Korea

**Bonjae Koo** – Department of Materials Science and Engineering, Korea Advanced Institute of Science and Technology (KAIST), Daejeon 34141, Republic of Korea

Jun Hyuk Kim – Department of Materials Science and Engineering, Korea Advanced Institute of Science and Technology (KAIST), Daejeon 34141, Republic of Korea

Complete contact information is available at:  
<https://pubs.acs.org/10.1021/acsami.0c05215>

### Author Contributions

J.K.K., Y.R.J., B.-J. K., and W.J. conceived and designed the project. J.K.K., B.K., and J.H.K. conducted the sample preparation and analysis. Y.R.J. and B.-J.K. undertook TEM analysis. S.K. measured the catalytic reactivity. All authors contributed to discussions of the results.

### Author Contributions

<sup>§</sup>These authors contributed equally

### Notes

The authors declare no competing financial interest.

## ACKNOWLEDGMENTS

B.-J. Kim and W. Jung acknowledge financial support from the Samsung Research Funding Center of Samsung Electronics under project number SRFC-MA1502-52.

## REFERENCES

- (1) Nishihata, Y.; Mizuki, J.; Akao, T.; Tanaka, H.; Uenishi, M.; Kimura, M.; Okamoto, T.; Hamada, N. Self-Regeneration of a Pd-Perovskite Catalyst for Automotive Emissions Control. *Nature* **2002**, *418* (6894), 164–167.
- (2) Newton, M. A. Dynamic Adsorbate/Reaction Induced Structural Change of Supported Metal Nanoparticles: Heterogeneous Catalysis and Beyond. *Chem. Soc. Rev.* **2008**, *37* (12), 2644–2657.
- (3) Oh, J.; Yoo, J. Do; Kim, K.; Yun, H. J.; Jung, W. C.; Bae, J. Negative Effects of Dopants on Copper–Ceria Catalysts for CO Preferential Oxidation Under the Presence of CO<sub>2</sub> and H<sub>2</sub>O. *Catal. Lett.* **2017**, *147* (12), 2987–3003.
- (4) Prieto, G.; Zečević, J.; Friedrich, H.; De Jong, K. P.; De Jongh, P. E. Towards Stable Catalysts by Controlling Collective Properties of Supported Metal Nanoparticles. *Nat. Mater.* **2013**, *12* (1), 34–39.
- (5) Li, Y.; Zhang, W.; Zheng, Y.; Chen, J.; Yu, B.; Chen, Y.; Liu, M. Controlling Cation Segregation in Perovskite-Based Electrodes for High Electro-Catalytic Activity and Durability. *Chem. Soc. Rev.* **2017**, *46* (20), 6345–6378.
- (6) Irvine, J. T. S.; Neagu, D.; Verbraeken, M. C.; Chatzichristodoulou, C.; Graves, C.; Mogensen, M. B. Evolution of the Electrochemical Interface in High-Temperature Fuel Cells and Electrolysers. *Nat. Energy* **2016**, *1* (1), 1–13.
- (7) Koo, B.; Kim, K.; Kim, J. K.; Kwon, H.; Han, J. W.; Jung, W. C. Sr Segregation in Perovskite Oxides: Why It Happens and How It Exists. *Joule* **2018**, *2* (8), 1476–1499.
- (8) Koo, B.; Kwon, H.; Kim, Y.; Seo, H. G.; Han, J. W.; Jung, W. Enhanced Oxygen Exchange of Perovskite Oxide Surfaces through Strain-Driven Chemical Stabilization. *Energy Environ. Sci.* **2018**, *11* (1), 71–77.
- (9) Cao, A.; Lu, R.; Veser, G. Stabilizing Metal Nanoparticles for Heterogeneous Catalysis. *Phys. Chem. Chem. Phys.* **2010**, *12* (41), 13499–13510.
- (10) Joo, S. H.; Park, J. Y.; Tsung, C. K.; Yamada, Y.; Yang, P.; Somorjai, G. A. Thermally Stable Pt/Mesoporous Silica Core-Shell Nanocatalysts for High-Temperature Reactions. *Nat. Mater.* **2009**, *8* (2), 126–131.
- (11) Cao, A.; Veser, G. Exceptional High-Temperature Stability through Distillation-like Self-Stabilization in Bimetallic Nanoparticles. *Nat. Mater.* **2010**, *9* (1), 75–81.
- (12) Lee, S.; Seo, J.; Jung, W. Sintering-Resistant Pt@CeO<sub>2</sub> Nanoparticles for High-Temperature Oxidation Catalysis. *Nanoscale* **2016**, *8* (19), 10219–10228.

(13) Choi, Y.; Cha, S. K.; Ha, H.; Lee, S.; Seo, H. K.; Lee, J. Y.; Kim, H. Y.; Kim, S. O.; Jung, W. C. Unravelling Inherent Electrocatalysis of Mixed-Conducting Oxide Activated by Metal Nanoparticle for Fuel Cell Electrodes. *Nat. Nanotechnol.* **2019**, *14* (3), 245–251.

(14) Kim, S.; Lee, S.; Jung, W. C. Sintering Resistance of Pt@SiO<sub>2</sub> Core-Shell Catalyst. *ChemCatChem* **2019**, *11* (18), 4653–4659.

(15) Jung, W.; Gu, K. L.; Choi, Y.; Haile, S. M. Robust Nanostructures with Exceptionally High Electrochemical Reaction Activity for High Temperature Fuel Cell Electrodes. *Energy Environ. Sci.* **2014**, *7* (5), 1685–1692.

(16) Neagu, D.; Oh, T. S.; Miller, D. N.; Ménard, H.; Bukhari, S. M.; Gamble, S. R.; Gorte, R. J.; Vohs, J. M.; Irvine, J. T. S. Nano-Socketed Nickel Particles with Enhanced Coking Resistance Grown in Situ by Redox Exsolution. *Nat. Commun.* **2015**, *6*, No. 8120.

(17) Neagu, D.; Kyriakou, V.; Roiban, I. L.; Aouine, M.; Tang, C.; Caravaca, A.; Kousi, K.; Schreur-Piet, I.; Metcalfe, I. S.; Vernoux, P.; van de Sanden, M. C. M.; Tsampas, M. N. In Situ Observation of Nanoparticle Exsolution from Perovskite Oxides: From Atomic Scale Mechanistic Insight to Nanostructure Tailoring. *ACS Nano* **2019**, *13*, 12996–13005.

(18) Neagu, D.; Tsekouras, G.; Miller, D. N.; Ménard, H.; Irvine, J. T. S. In Situ Growth of Nanoparticles through Control of Non-Stoichiometry. *Nat. Chem.* **2013**, *5* (11), 916–923.

(19) Oh, T. S.; Rahani, E. K.; Neagu, D.; Irvine, J. T. S.; Shenoy, V. B.; Gorte, R. J.; Vohs, J. M. Evidence and Model for Strain-Driven Release of Metal Nanocatalysts from Perovskites during Exsolution. *J. Phys. Chem. Lett.* **2015**, *6* (24), 5106–5110.

(20) Jo, Y. R.; Koo, B.; Seo, M. J.; Kim, J. K.; Lee, S.; Kim, K.; Han, J. W.; Jung, W. C.; Kim, B. J. Growth Kinetics of Individual Co Particles Ex-Solved on SrTi<sub>0.75</sub>Co<sub>0.25</sub>O<sub>3–3</sub> Polycrystalline Perovskite Thin Films. *J. Am. Chem. Soc.* **2019**, *141* (16), 6690–6697.

(21) Papaioannou, E. I.; Neagu, D.; Ramli, W. K. W.; Irvine, J. T. S.; Metcalfe, I. S. Sulfur-Tolerant, Exsolved Fe–Ni Alloy Nanoparticles for CO Oxidation. *Top. Catal.* **2019**, *62* (17), 1149–1156.

(22) Cui, D.; Qiu, Y.; Lv, Y.; Li, M.; Zhang, S.; Tippayawong, N.; Zeng, D.; Xiao, R. A High-Performance Oxygen Carrier with High Oxygen Transport Capacity and Redox Stability for Chemical Looping Combustion. *Energy Convers. Manage.* **2019**, *202*, 112209.

(23) Madsen, B. D.; Kobsiriphat, W.; Wang, Y.; Marks, L. D.; Barnett, S. A. Nucleation of Nanometer-Scale Electrocatalyst Particles in Solid Oxide Fuel Cell Anodes. *J. Power Sources* **2007**, *166* (1), 64–67.

(24) Kousi, K.; Neagu, D.; Bekris, L.; Papaioannou, E. I.; Metcalfe, I. S. Methane Conversion Endogenous Nanoparticles Strain Perovskite Host Lattice Providing Oxygen Capacity and Driving Oxygen Exchange and CH<sub>4</sub> Conversion to Syngas. *Angew. Chem., Int. Ed.* **2020**, *59*, 2510–2519.

(25) Kwon, O.; Sengodan, S.; Kim, K.; Kim, G.; Jeong, H. Y.; Shin, J.; Ju, Y. W.; Han, J. W.; Kim, G. Exsolution Trends and Co-Segregation Aspects of Self-Grown Catalyst Nanoparticles in Perovskites. *Nat. Commun.* **2017**, *8*, 1–7.

(26) Katz, M. B.; Graham, G. W.; Duan, Y.; Liu, H.; Adamo, C.; Schlom, D. G.; Pan, X. Self-Regeneration of Pd-LaFeO<sub>3</sub> Catalysts: New Insight from Atomic-Resolution Electron Microscopy. *J. Am. Chem. Soc.* **2011**, *133* (45), 18090–18093.

(27) Gao, Y.; Chen, D.; Saccoccio, M.; Lu, Z.; Ciucci, F. From Material Design to Mechanism Study: Nanoscale Ni Exsolution on a Highly Active A-Site Deficient Anode Material for Solid Oxide Fuel Cells. *Nano Energy* **2016**, *27*, 499–508.

(28) Li, X.; Dai, L.; He, Z.; Meng, W.; Li, Y.; Wang, L. In Situ Exsolution of PdO Nanoparticles from Non-Stoichiometric LaFeP<sub>d<sub>0.05</sub>O<sub>3+Δ</sub></sub> Electrode for Impedanceometric NO<sub>2</sub> Sensor. *Sens. Actuators, B* **2019**, *298*, 126827.

(29) Hua, B.; Li, M.; Sun, Y. F.; Zhang, Y. Q.; Yan, N.; Chen, J.; Thundat, T.; Li, J.; Luo, J. L. A Coupling for Success: Controlled Growth of Co/CoO<sub>x</sub> Nanoshoots on Perovskite Mesoporous Nanofibres as High-Performance Trifunctional Electrocatalysts in Alkaline Condition. *Nano Energy* **2017**, *32*, 247–254.

- (30) Xu, M.; Wang, W.; Zhong, Y.; Xu, X.; Wang, J.; Zhou, W.; Shao, Z. Enhancing the Triiodide Reduction Activity of a Perovskite-Based Electrocatalyst for Dye-Sensitized Solar Cells through Exsolved Silver Nanoparticles. *J. Mater. Chem. A* **2019**, *7* (29), 17489–17497.
- (31) Shen, X.; Chen, T.; Bishop, S. R.; Perry, N. H.; Tuller, H. L.; Sasaki, K. Redox Cycling Induced Ni Exsolution in  $\text{Gd}_{0.1}\text{Ce}_{0.8}\text{Ni}_{0.1}\text{O}_{2-x}$  ( $\text{Sr}_{0.9}\text{La}_{0.1}$ )<sub>0.9</sub> $\text{Ti}_{0.9}\text{Ni}_{0.1}\text{O}_3$  Composite Solid Oxide Fuel Cell Anodes. *J. Power Sources* **2017**, *370*, 122–130.
- (32) Kim, K. J.; Rath, M. K.; Kwak, H. H.; Kim, H. J.; Han, J. W.; Hong, S. T.; Lee, K. T. A Highly Active and Redox-Stable  $\text{SrGdNi}_{0.2}\text{Mn}_{0.8}\text{O}_{4\pm\delta}$  Anode with in Situ Exsolution of Nanocatalysts. *ACS Catal.* **2019**, *9* (2), 1172–1182.
- (33) Yu, J.; Zhang, L.; Qian, J.; Zhu, Z.; Ni, S.; Liu, G.; Xu, X. In Situ Exsolution of Silver Nanoparticles on  $\text{AgTaO}_3$ - $\text{SrTiO}_3$  Solid Solutions as Efficient Plasmonic Photocatalysts for Water Splitting. *Appl. Catal., B* **2019**, *256*, 117818.
- (34) Zhu, T.; Troiani, H.; Moggi, L. V.; Santaya, M.; Han, M.; Barnett, S. A. Exsolution and Electrochemistry in Perovskite Solid Oxide Fuel Cell Anodes: Role of Stoichiometry in  $\text{Sr}(\text{Ti}, \text{Fe}, \text{Ni})\text{O}_3$ . *J. Power Sources* **2019**, *439*, 227077.
- (35) Gao, Y.; Wang, J.; Lyu, Y. Q.; Lam, K.; Ciucci, F. In Situ Growth of  $\text{Pt}_3\text{Ni}$  Nanoparticles on an A-Site Deficient Perovskite with Enhanced Activity for the Oxygen Reduction Reaction. *J. Mater. Chem. A* **2017**, *5* (14), 6399–6404.
- (36) Otto, S. K.; Kousi, K.; Neagu, D.; Bekris, L.; Janek, J.; Metcalfe, I. S. Exsolved Nickel Nanoparticles Acting as Oxygen Storage Reservoirs and Active Sites for Redox  $\text{CH}_4$  Conversion. *ACS Appl. Energy Mater.* **2019**, *2* (10), 7288–7298.
- (37) Nenning, A.; Fleig, J. Electrochemical XPS Investigation of Metal Exsolution on SOFC Electrodes: Controlling the Electrode Oxygen Partial Pressure in Ultra-High-Vacuum. *Surf. Sci.* **2019**, *680*, 43–51.
- (38) Chen, Y.; Chen, Y.; Ding, D.; Ding, Y.; Choi, Y. M.; Zhang, L.; Yoo, S.; Chen, D.; DeGlee, B.; Xu, H.; Lu, Q.; Zhao, B.; Vardar, G.; Wang, J.; Bluhm, H.; Crumlin, E. J.; Yang, C.; Liu, J.; Yildiz, B.; Liu, M. A Robust and Active Hybrid Catalyst for Facile Oxygen Reduction in Solid Oxide Fuel Cells. *Energy Environ. Sci.* **2017**, *10* (4), 964–971.
- (39) Zhu, Y.; Zhou, W.; Ran, R.; Chen, Y.; Shao, Z.; Liu, M. Promotion of Oxygen Reduction by Exsolved Silver Nanoparticles on a Perovskite Scaffold for Low-Temperature Solid Oxide Fuel Cells. *Nano Lett.* **2016**, *16* (1), 512–518.
- (40) Joo, S.; Kwon, O.; Kim, K.; Kim, S.; Kim, H.; Shin, J.; Jeong, H. Y.; Sengodan, S.; Han, J. W.; Kim, G. Cation-Swapped Homogeneous Nanoparticles in Perovskite Oxides for High Power Density. *Nat. Commun.* **2019**, *10* (1), 1–9.
- (41) Gao, Y.; Lu, Z.; You, T. L.; Wang, J.; Xie, L.; He, J.; Ciucci, F. Energetics of Nanoparticle Exsolution from Perovskite Oxides. *J. Phys. Chem. Lett.* **2018**, *9* (13), 3772–3778.
- (42) Kim, K. J.; Han, H.; Defferriere, T.; Yoon, D.; Na, S.; Kim, S. J.; Dayaghi, A. M.; Son, J.; Oh, T. S.; Jang, H. M.; Choi, G. M. Facet-Dependent in Situ Growth of Nanoparticles in Epitaxial Thin Films: The Role of Interfacial Energy. *J. Am. Chem. Soc.* **2019**, *141* (18), 7509–7517.
- (43) Han, H.; Park, J.; Nam, S. Y.; Kim, K. J.; Choi, G. M.; Parkin, S. S. P.; Jang, H. M.; Irvine, J. T. S. Lattice Strain-Enhanced Exsolution of Nanoparticles in Thin Films. *Nat. Commun.* **2019**, *10* (1), 1–8.
- (44) Kwak, N. W.; Jeong, S. J.; Seo, H. G.; Lee, S.; Kim, Y. J.; Kim, J. K.; Byeon, P.; Chung, S. Y.; Jung, W. C. In Situ Synthesis of Supported Metal Nanocatalysts through Heterogeneous Doping. *Nat. Commun.* **2018**, *9* (1), 1–8.
- (45) Lai, K. Y.; Manthiram, A. Evolution of Exsolved Nanoparticles on a Perovskite Oxide Surface during a Redox Process. *Chem. Mater.* **2018**, *30* (8), 2838–2847.
- (46) Kitakami, O.; Sato, H.; Shimada, Y.; Sato, F.; Tanaka, M. Size Effect on the Crystal Phase of Cobalt Fine Particles. *Phys. Rev. B: Condens. Matter Mater. Phys.* **1997**, *56* (21), 13849–13854.
- (47) Dinega, D. P.; Bawendi, M. G. A Solution-Phase Chemical Approach to a New Crystal Structure of Cobalt. *Angew. Chem., Int. Ed.* **1999**, *38* (12), 1788–1791.
- (48) Oh, T. S.; Tokpanov, Y. S.; Hao, Y.; Jung, W.; Haile, S. M. Determination of Optical and Microstructural Parameters of Ceria Films. *J. Appl. Phys.* **2012**, *112* (10), 103535.
- (49) JCPDS 79–0176 (STO), JCPDS 05-0727 (HCP), and JCPDS 15-0806 (FCC).
- (50) Porter, D. A.; Easterling, K. E. *Phase Transformations in Metals and Alloys*, 2nd ed.; Chapman & Hall, 1992.